Competing interaction induced phase diagram and phase transition in artificial triangular spin ice

Haifeng Lou [1,*] Wen-Cheng Yue,[2,*] Zixiong Yuan,[2] Peiyuan Huang,[2] Yan Chen,[3]
Yong-Lei Wang [2,†] Shilei Zhang [1,‡] and Dong Shi [1,§]

[1]*School of Physical Science and Technology, Shanghai Tech University, Shanghai 200031, China*
[2]*School of Electronic Science and Engineering, Nanjing University, Nanjing 210023, China*
[3]*Research Center for Analysis and Measurement, Fudan University, Shanghai 200438, China*

Competing interactions are the simultaneous presence of conflicting coupling forces in a system, which can lead to the emergence of rich physical properties and phenomena. We have studied artificial spin ices composed of single-domain nanomagnets on triangular arrays using magnetic force microscopy and Monte Carlo simulations. A phase diagram with three distinct phases is obtained analytically through tuning the interaction between local neighboring spins continuously. These phases and phase boundaries are precisely reproduced by experimental data, providing strong evidence for the success of our theoretical model. Further to this, a subsequent study reveals that incorporating long-range interactions results in different phase boundaries. This conclusion is further confirmed by another experiment where a phase transition behavior is observed when the spin correlation within the system exceeds the neighbors within a triangular vertex. These findings indicate that further neighbor interactions in artificial triangular array can significantly affect the magnetic phases of the system, showing significant differences from other geometry-based artificial spin ices.

I. INTRODUCTION

Artificial spin ice has been studied for decades as an ideal platform for investigating the geometry frustration-induced phenomena in spin systems [1–21]. These artificially designed systems offer advantages such as tunability and flexibility, allowing for the exploration of geometry frustration in a highly controlled manner. In frustrated magnetism systems, frustration arises from the competition between different interactions among neighboring spins. To explore the phase diagram of such systems, a conventional approach involves adjusting the coupling strength ratio between neighbors at different distances [22–29]. The application of lithographic techniques in artificial spin ice systems makes such explorations possible. Additionally, nanoimaging tools like magnetic force microscopy (MFM) and x-ray magnetic circular dichroism enable straightforward examination of macro spin states in real space [1–3,9–12,16,18,19,27–33]. The combination of these advantages renders artificial spin ice an ideal platform for testing theoretical models on diverse geometries [1,3,34–38]. For instance, in the case of dipolar square ice, collective magnetic phenomena such as spin liquid states and Coulomb phases have been experimentally observed by varying the vertical shift between the two sublattices of the pattern [39,40].

We investigate an array consisting of nanomagnet islands on a triangular lattice through experimental and simulation methods. We examine the phase variation as the coupling strength of different spin pairs is continuously tuned. Three distinct magnetic phases arise within the system when considering the coupled interactions J_1 (nearest neighbor), J_2 (second nearest neighbor), and J_3 (third nearest neighbor) only. These predicted phases and phase boundaries are precisely reproduced by experimental data, which evidence the success of the J_1-J_2-J_3 model. Furthermore, we extend our study by incorporating interactions among neighbors beyond J_1, J_2, and J_3. Both simulation and analytical results show significant changes in the phase boundaries when these additional interactions are taken into account. To validate these predictions, we design and conduct another experiment in which a series of triangular arrays with varying spin correlations are examined. A phase transition signature is observed near the shifted phase boundary. This phenomenon aligns with the results obtained from Monte Carlo simulations, providing strong evidence for the dependence of phase boundaries on spin correlations in a triangular array. All these finding demonstrate the rich physics exhibited by artificial triangular ice.

II. THE MODEL AND PHASE DIAGRAM

The nanomagnets in the triangular array are elongated along the vertical direction and interact with each other through dipolar interactions. Therefore, they can be effectively treated as Ising spins. For dipolar interactions, when two magnetic moments $\vec{\mu}_1$ and $\vec{\mu}_2$ are Ising like and separated by a distance r, as shown in Fig. 1(a), the interaction energy between the two moments can be expressed as a function of θ and r,

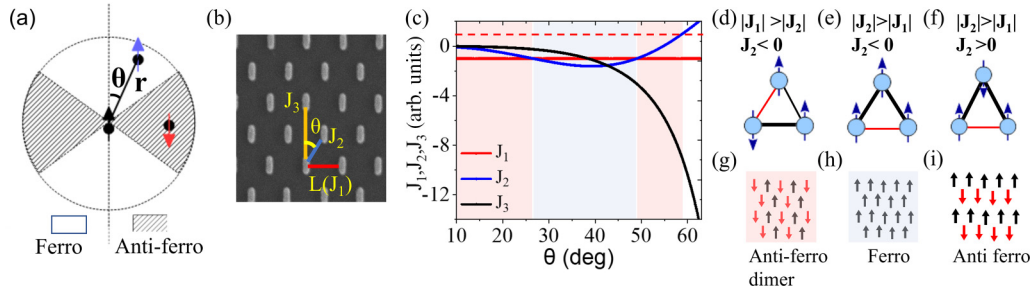$$E_{\uparrow\uparrow} = \frac{D}{r^3}(1 - 3\cos^2\theta) \qquad (1)$$

FIG. 1. (a) The diagram shows that the dipolar interaction favors ferromagnetic coupling or antiferromagnetic coupling between two magnetic moments based on the angle θ. (b) A SEM image of a section of one triangular spin ice array with constant space L (J_1) and θ ($L = 280$ nm, $\theta = 20°$). (c) Variation in J_1, J_2, and J_3 as a function of θ. The shaded area denotes possible magnetic order in this region. Inset: The definition of J_1, J_2, J_3, and θ in a triangular spin array are schematically shown. (d)–(f) Different possible magnetic orders that are predicted depending on the relative coupling strength among J_1, J_2, and J_3. The red line indicates the moments are staying in an energetically unfavorable alignment, while the black lines indicate the moments are staying in an energetically favorable alignment. (g)–(i) The possible magnetic phases that are predicted based on the local spin configurations given by (d), (e) and (f), respectively.

and

$$E_{\uparrow\downarrow} = \frac{D}{r^3}(-1 + 3\cos^2\theta), \tag{2}$$

where θ is the angle between the vertical direction and the vector $\vec{r}$. The dipolar energy, denoted as $E_{\uparrow\uparrow}$ or $E_{\uparrow\downarrow}$, corresponds to the energy when the two moments are parallel or antiparallel, respectively. The constant $D = \mu_0\mu^2/4\pi$. It is noteworthy that when $E_{\uparrow\uparrow} = E_{\uparrow\downarrow}$, the angle θ is 54.7°. When we place the spins in a polar coordinate system, as illustrated in Fig. 1(a), the entire area can be divided into two regions. The dipolar interaction favors parallel or antiparallel alignment depending on the relative position of the other spin with respect to a reference spin located at the origin. Based on this property, when considering macro spins in a triangular array, the neighboring couplings can be defined as J_1, J_2, and J_3 based on their relative positions, as shown in Fig. 1(b). By maintaining a fixed spacing between the elements along the horizontal direction, i.e., keeping J_1 constant, and varying the distance between elements along the vertical direction, we can continuously adjust the couplings J_2 and J_3 as a function of θ. These variations are depicted in Fig. 1(c). Assuming $J_1 = -1$, the competition among J_1, J_2, and J_3 gives rise to diverse magnetic phases that are θ dependent.

A. When $\theta < 26.8°$, $|J_1| > |J_2|$

When J_1 is dominant, the neighboring spins oriented along the horizontal axis prefer to be antiparallel, resulting in frustration for the spins situated at the diagonal positions, which prefer parallel alignment. This dominance of J_1 gives rise to a preferred local spin configuration, as illustrated in Fig. 1(d). This constraint leads to the ordering of spins along the horizontal direction, forming antiparallel aligned spin chains. Based on this alignment, when J_3 is introduced, the coupling between spin chains along the vertical direction is enhanced. This coupling enhancement offers an anisotropy along the vertical direction and reduces the degeneracy of the spin chains. As a consequence, the ground state of the system manifests as an antiferromagnetic dimer phase, as illustrated in Fig. 1(g).

B. When $26.8° < \theta < 49.1°$, $|J_2| > |J_1|$

When J_2 is dominant, the local spin configuration prefers to align in the same direction, as illustrated in Fig. 1(e). This alignment results in the entire system favoring a ferromagnetic state, as illustrated in Fig. 1(h). In this case, the influence of J_3 is disregarded as it does not introduce any frustration into the system.

C. When $49.1° < \theta < 58.9°$, $|J_1| > |J_2|$

In this region, J_1 wins the competition against J_2 and does not frustrate with J_3. As a result, the system prefers to be in an antiferromagnetic dimer phase again.

D. When $58.9° < \theta$, $|J_2| > |J_1|$, $J_2 > 0$

In this case, with $J_2 > 0$ and dominant, the spin pairs along the diagonal orientations prefer to be antiparallel. Conversely, the spin pairs along the horizontal directions are compelled to be parallel aligned. As a result, the preferred local spin configuration is illustrated in Fig. 1(f). The overall preferred magnetic phase of the system is an antiferromagnetic state, as illustrated in Fig. 1(i). It is worth noting that in all the cases just discussed, the frustration and resulting magnetic phases primarily arise from the competition between J_1 and J_2. The presence of J_3 does not introduce frustration, but instead provides an anisotropy along the vertical direction, leading to stripelike phases. As a result, the three magnetic phases discussed earlier exhibit a twofold degeneracy.

III. EXPERIMENT AND ANALYSIS RESULTS

To validate the J_1-J_2-J_3 model experimentally, we fabricated a series of triangular patterns consisting of permalloy nanomagnets on a silicon substrate. These patterns were designed with different angles θ, including 20°, 22.5°, 26°, 30°, 40°, 50°, and 56°. The spacing between islands in each row is kept at 280 nm and each nanomagnet has dimensions of $150 \times 50 \times 20$ nm. To investigate the antiferromagnetic phase in the J_1-J_2-J_3 model, the pattern with angle $\theta > 58.9°$ needs to be examined. Nevertheless, the elements in such a pattern
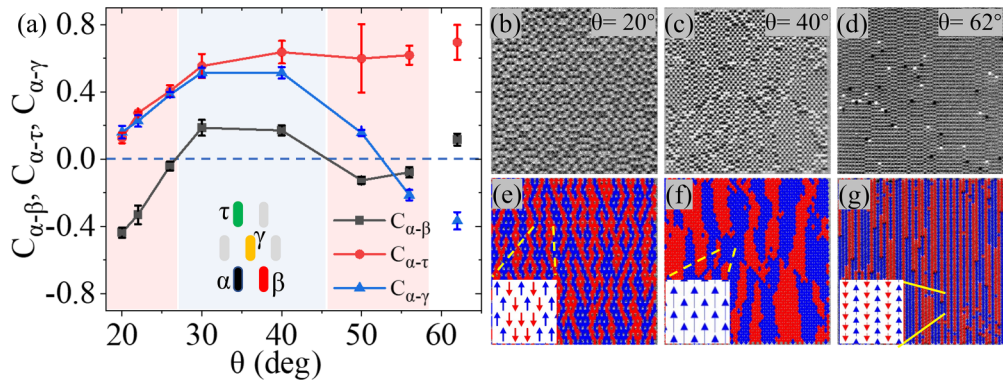
FIG. 2. Phase diagram identified from the experimental data. (a) Magnetic phases identified from the MFM images based on the order parameter analysis of three spin pairs $\alpha\beta$, $\alpha\gamma$, and $\alpha\delta$. Inset: Sketch of the spin pairs. The data point at $\theta = 62°$ is not connected due to the use of different lattice spacing. The colored areas denote the magnetic phase boundaries, where red, blue, and white denote the antiferromagnetic dimer phase, ferromagnetic phase, and antiferromagnetic phase, respectively. (b)–(d) Typical MFM images of patterns with different angles θ: 20°, 40°, and 62°, respectively. (e)–(g) Color-mapped MFM images corresponding to (b), (c), and (d), respectively. Blue and red represent spins pointing in different directions. Insets: Magnified spin configuration maps from a specific area within the MFM images.

would touch, or even overlap, if a lattice constant of 280-nm is used. To avoid this situation, the element size needs to be reduced, which poses challenges for electron beam lithography and MFM. In this work, we fabricated the pattern with an angle of $\theta = 62°$, but with a slightly larger spacing (360 nm) between islands in each row to address these challenges. Each pattern is designed with a size of 10×10 μm. The fabrication process involves the use of electron-beam lithography, followed by a liftoff process to create the desired patterns on the substrate. The patterns are not capped with any coating layer. In order to find the low-energy state of the system, a field demagnetization protocol is employed. An in-plane magnetic field is applied, gradually ramping down from 1000 Gs to 0 G in 72 hours, while the sample is rotated in-plane at 2000 rpm. The spin configurations of each pattern are then imaged using MFM. All the experimental information, including scanning electron microscopy (SEM) images and MFM images of arrays with different angles can be found in Supplemental Material Figs. S3–S6 [41].

Due to shape anisotropy, the magnetization of each nanomagnet points along its long axis. Therefore, the MFM scanning result of each nanomagnet would consist of two points with different colors. To visualize the results, a two-color mapping technique is utilized, where blue and red represent the different spin orientations. Figure 2(b)–2(d) presents three typical MFM images obtained from patterns with θ angles of 20°, 40°, and 62°, respectively. The corresponding mapping results of these MFM images are displayed in Fig. 2(e)–2(g), respectively. The feature of these mapping results effectively illustrates the variation in the coupling strength. For example, in the low θ region, where J_2 and J_3 are weak compared to J_1, the system exhibits weak ordering along the vertical direction but strong ordering along the horizontal direction. This tendency favors the formation of antiferromagnetic spin chains, which is reflected in the mapping result of the pattern with $\theta = 20°$. On the other hand, the color mapping result of the pattern with $\theta = 40°$ reveals the presence of large ferromagnetic domains. This behavior is consistent with the variation of J_2, as the domain formation in a triangular array is influenced by the competition between

J_1 and J_2. Hence, the domain width reaches its maximum at $\theta = 40°$. Furthermore, in the high θ region, where J_3 is strong, providing an anisotropy along the vertical direction, the spin configurations exhibit a stripelike feature. This is clearly visible in the color mapping result of the pattern with $\theta = 62°$. Detailed domain length estimation results are displayed in Supplemental Material Fig. S2 [41], indicating that the domain length increases with the angle θ. To identify the magnetic phases from the MFM images more accurately, we calculate the spin-spin correlation of three spin pairs along the horizontal, diagonal, and vertical directions, denoted by $C_{\alpha\beta}$, $C_{\alpha\gamma}$, and $C_{\alpha\delta}$, respectively. The correlation coefficient $C_{ij} = \langle \sigma_i \cdot \sigma_j \rangle$, where $\langle \rangle$ denotes the average over the entire system for all ij pairs; $\sigma_i \cdot \sigma_j = 1$ if spin i is parallel to spin j, and -1 otherwise. According to the phase definitions, the criteria for determining the magnetic phases are as follows:

(1) Antiferromagnetic dimer phase if $C_{\alpha\beta} < 0$.

(2) Ferromagnetic phase if $C_{\alpha\beta} > 0$ and $C_{\alpha\gamma} > 0$.

(3) Antiferromagnetic phase if $C_{\alpha\beta} > 0$ and $C_{\alpha\gamma} < 0$.

The Greek letters α, β, γ, and δ denote spin pairs along different directions, as illustrated in the inset of Fig. 2(a). The value of the correlation coefficients $C_{\alpha\beta}$, $C_{\alpha\gamma}$, and $C_{\alpha\delta}$ extracted from the MFM images are shown in Fig. 2(a). According to the criteria just listed, four different regions can be identified, corresponding to three distinct magnetic phases. When comparing the phase boundaries obtained from the experimental data with those depicted in Fig. 1(c), we observe a significant agreement between the two. This suggests that the J_1-J_2-J_3 model captures the essential physics of the system. To confirm this conclusion further, we also performed micromagnetic simulation [42] on nanomagnets in a triangular array with the same angles that have been used in the experiments. For each array, we calculated the total energy of every possible spin configuration and listed the preferred energy state (see Supplemental Material Fig. S1 [41]). The micromagnetic simulation results coincide with the predicted one in the J_1-J_2-J_3 model and the experimental results. This agreement shows the success of the point dipole model approximation and also indicates that the interactions beyond J_1, J_2, and J_3, do not play prominent roles in the demagnetized states.
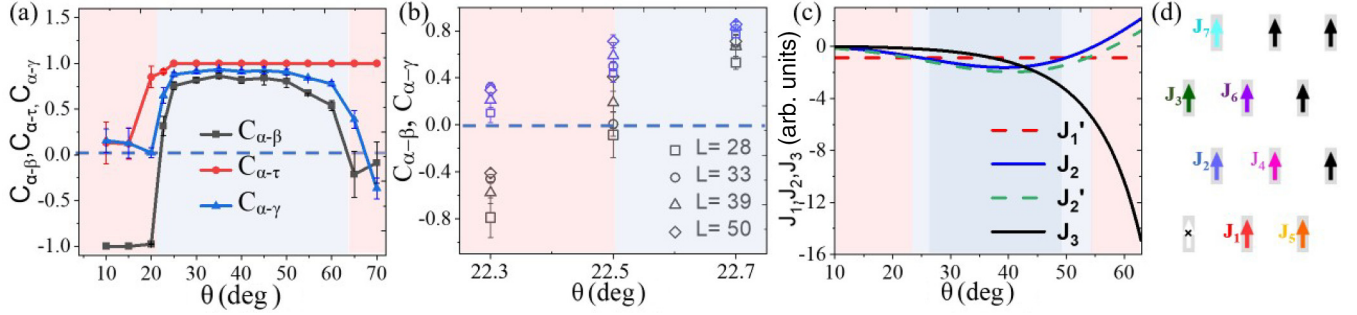
FIG. 3. Phase diagram identified from the Monte Carlo simulations and theoretical method. (a) Magnetic phases identified from the Monte Carlo simulation results of the quenching process for patterns with different angles θ. All the neighbor interactions are considered in the simulations. (b) Monte Carlo simulation for magnetic phase order parameter measurements around $\theta = 22.5°$ with system size $L = 28, 33, 39$, and 50. The black symbols denote the order parameter $C_{\alpha\beta}$ and the blue symbols denote the order parameter $C_{\alpha\gamma}$. (c) Variation in the effective J'_1, J'_2, J_2, and J_3 as a function of θ. The dark blue area represents the ferromagnetic phase predicted based on the J_1-J_2-J_3 model. (d) Definition of the spin neighbors up to the seventh nearest neighbor.

IV. FURTHER NEIGHBOR INTERACTIONS STUDY

In order to gain a deeper understanding of the system's behavior and to explore the influence of additional neighbor interactions, we proceeded with our study by considering further interactions among neighboring spins. To test the influence of further neighbor interactions, we performed Monte Carlo simulations on a triangular array using the following Hamiltonian:

$$H = \frac{1}{2}A \sum_{ij(i \neq j)}^{N} \frac{\mu_0}{4\pi r_{ij}^3} \left[\hat{\mu}_i \cdot \hat{\mu}_j - \frac{3}{r_{ij}^2}(\hat{\mu}_i \cdot \hat{r}_{ij})(\hat{\mu}_j \cdot \hat{r}_{ij}) \right], \quad (3)$$

where μ_0 represents the permeability of the free space, $\hat{\mu}_i$ and $\hat{\mu}_j$ denote the magnetic moments of spin i and spin j in the system, and $\hat{r}_{ij}$ is the distance between spin $\hat{\mu}_i$ and $\hat{\mu}_j$. The parameter A represents the coupling strength between the spins. The simulation is performed on an $L \times L$ lattice, where $L = 35$ and all spin pair interactions are taken into account. A single spin flip algorithm and a simulated annealing procedure is used to explore the low-energy states. The magnetic phase obtained from simulation are identified based on the spin correlation calculation of $C_{\alpha\beta}$, $C_{\alpha\gamma}$, and $C_{\alpha\delta}$, as described earlier. The results are shown in Fig. 3(a). It worth noting that we do not perform simulations for angles $\theta < 10°$ and $\theta > 65°$, as in both cases the ordered spins tend to form spin chains in rows or columns that are weakly coupled to each other. Compared to the phase diagram obtained from the J_1-J_2-J_3 model, the inclusion of the further neighbor interactions significantly broadens the ferromagnetic phase regions while suppressing the other phase regions. The phase boundary between the antiferromagnetic dimer phase and the ferromagnetic phase shift to $\theta = 22.5°$, while the phase boundary between the ferromagnetic phase and antiferromagnetic dimer phase shift to $\theta = 64°$. A fine-angle-range of Monte Carlo simulation results around $\theta = 22.5°$ is displayed in Fig. 3(b), where $C_{\alpha\beta}$ and $C_{\alpha\gamma}$ for $\theta = 22.3°$, $22.5°$, and $22.7°$ are calculated for the system size $L = 28, 33, 39$, and 50. For $\theta = 22.3°$ and $22.7°$, the magnetic phase remains stable as the system size increases. This result indicates that the phase boundary is fixed within the range of $0.2°$ around $22.5°$. For $\theta = 22.5°$, the magnetic phase varies from the antiferromagnetic dimer

phase to the ferromagnetic phase as the system size increases. This indicates that the size effect needs to be considered when the magnetic phase is close to the phase boundary. The discrepancy of the phase boundary between the theory and the Monte Carlo simulation indicates that when further neighbor interactions are considered, the vertex model is not suitable to describe the triangular system.

To understand this phenomenon better, we modified the J_1-J_2-J_3 model by considering interactions up to the seventh nearest neighbor. The neighboring spins are defined as shown in Fig. 3(d). We renormalize the J_1 and J_2 interactions, resulting in effective J'_1 and J'_2: $J'_1 = J_1 + J_5$ and $J'_2 = J_2 + J_4 + J_6 + J_7$. The intersection point of J'_1 and J'_2 redefine the ferromagnetic phase region and antiferromagnetic dimer phase region. As shown in Fig. 3(c), the ferromagnetic phase expands on both sides compared to the phase obtained from the J_1-J_2-J_3 model. This is not surprising. Let us examine the state at the expanded area of the ferromagnetic phase region. If we place all the spins in the ferromagnetic state, when the neighbor interactions beyond J_1, J_2, and J_3 are incorporated, the energy gain from neighboring spins in the ferromagnetic region can compensate for the energy cost from the neighboring spins in the antiferromagnetic region. This is due to the fact that, for an individual spin, the density and the coupling strength of neighboring spins in the ferromagnetic region are generally higher than in the antiferromagnetic region across most of the θ range in the phase diagram, as can be inferred from Fig. 1(a). Consequently, the system tends to favor a ferromagnetic state as a result of this energy compensation. This implies that the phase boundary is not solely determined by the extent of the pattern deformation, but also is related to the spin correlation of the system. Since dipole interactions are long range, incorporating more interactions with neighboring spins allows the system to obtain greater energy compensation, leading to a shifting of the phase boundary. Based on this assumption, if we examine the state near the phase boundary, an increase in spin correlation can lead the system to cross the phase boundary, leading to a phase transition. This phenomenon can be observed during a cooling process, where the spin correlations increase as the system gradually cools.
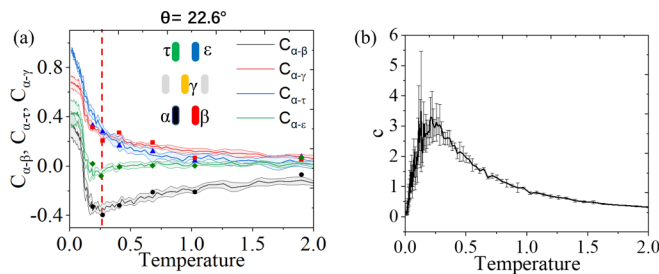
FIG. 4. Experimental and simulation results of a quenching process. (a) Spin correlation coefficient variation as a function of temperature. The data are obtained from Monte Carlo simulations of a quenching process and are fitted to the experimental data for patterns with different lattice constants (ranging from 240 nm to 680 nm) but with a constant angle θ (22.6°). The vertical red dashed line represents the experimental data highlighted in Fig. 2. (b) Specific capacity as a function of temperature obtained from the same Monte Carlo simulation results in (a).

To validate this assumption, another experiment is conducted using triangular arrays with a fixed angle but various lattice constants. The lattice constants of the patterns vary from 240 nm to 680 nm. The field demagnetization protocol is the same as mentioned earlier, and the spin correlation of the system with different lattice constants is calculated and compared with the results from a Monte Carlo simulation of a quenching process. Here, the angle θ is chosen to be 22.6°, as the ground state of the system with this angle is in the vicinity of the phase boundary between the antiferromagnetic dimer phase and the ferromagnetic phase. By selecting this particular angle, the system is in a critical regime, where a slight change in the lattice constant can significantly affect the spin correlations and phase behavior. As shown in Fig. 4(a), the spin correlations extracted from the experiments show good agreement with the results obtained from the Monte Carlo simulation at different temperature ranges. $C_{\alpha\beta}$ decreases as the temperature cools until it reaches a minimum around $T = 0.22$, and then ramps up to a positive value. According to the criteria mentioned earlier, this indicates that the system

undergoes a phase transition from the antiferromagnetic dimer phase to the ferromagnetic phase. This phase transition is also identified by the analysis of the heat capacity, as shown in Fig. 4(b), where a peak arises at the same temperature position as the turning point in Fig. 4(a), indicating a second-order phase transition. Although the cooling process is accompanied by the growth of the spin correlation length, $C_{\alpha\varepsilon}$ remains almost constant before the phase transitions occur. This suggest that the neighboring spins have not built correlations up to the sixth nearest neighbor before the phase transition happened. This is why the J_1-J_2-J_3 model can coincide with the experimental results, as the neighbor interactions are still limited within this scope. On the other hand, the appearance of the turning point of $C_{\alpha\beta}$ and $C_{\alpha\varepsilon}$ indicates that the coupled neighbors extend beyond the scope of the J_1-J_2-J_3 model. This turning point can be deemed a sign of an incipient phase transition occurring in the system.

For a triangular lattice, the system favoring a magnetic phase depends on the lattice aspect ratio. This unique characteristic enables the tuning of the preferred moment configuration through deliberate design, a feature that holds substantial promise for various device applications. Furthermore, the influence of distant neighbors and indirect interactions can have a profound impact on the magnetic phases and phase boundaries within a system. When the structure is intentionally designed to remain close to these phase boundaries, it becomes susceptible to local magnetic fields, offering a versatile means of manipulating the moment configuration. Overall, this study highlights the complex nature of triangular spin arrays and their phase transitions. It opens up avenues for further research to explore the impact of extended neighbor interactions and develop a more comprehensive understanding of the physics underlying these systems.

[1] R. F. Wang, C. Nisoli, R. S. Freitas, J. Li, W. McConville, B. J. Cooley, M. S. Lund, N. Samarth, C. Leighton, V. H. Crespi, and P. Schiffer, Artificial 'spin ice' in a geometrically frustrated lattice of nanoscale ferromagnetic islands, Nature (London) **439**, 303 (2006).

[2] M. Tanaka, E. Saitoh, H. Miyajima, T. Yamaoka, and Y. Iye, Magnetic interactions in a ferromagnetic honeycomb nanoscale network, Phys. Rev. B **73**, 052411 (2006).

[3] Y. Qi, T. Brintlinger, and J. Cumings, Direct observation of the ice rule in an artificial kagome spin ice, Phys. Rev. B **77**, 094418 (2008).

[4] J. P. Morgan, A. Stein, S. Langridge, and C. H. Marrows, Thermal ground-state ordering and elementary excitations in artificial magnetic square ice, Nat. Phys. **7**, 75 (2010).

[5] J. Li, X. Ke, S. Zhang, D. Garand, C. Nisoli, P. Lammert, V. H. Crespi, and P. Schiffer, Comparing artificial frustrated magnets

by tuning the symmetry of nanoscale permalloy arrays, Phys. Rev. B **81**, 092406 (2010).

[6] Z. Budrikis, J. P. Morgan, J. Akerman, A. Stein, P. Politi, S. Langridge, C. H. Marrows, and R. L. Stamps, Disorder strength and field-driven ground state domain formation in artificial spin ice: Experiment, simulation, and theory, Phys. Rev. Lett. **109**, 037203 (2012).

[7] C. Nisoli, R. Moessner, and P. Schiffer, Colloquium: Artificial spin ice: designing and imaging magnetic frustration, Rev. Mod. Phys, **85**, 1473, (2013).

[8] V. S. Bhat, J. Sklenar, B. Farmer, J. Woods, J. T. Hastings, S. J. Lee, J. B. Ketterson, and L. E. DeLong, Controlled magnetic reversal in permalloy films patterned into artificial quasicrystals, Phys. Rev. Lett. **111**, 077201 (2013).

[9] I. Gilbert, G. W. Chern, S. Zhang, L. O'Brien, B. Fore, C. Nisoli, and P. Schiffer, Emergent ice rule and magnetic charge

screening from vertex frustration in artificial spin ice, Nat. Phys. **10**, 670 (2014).

[10] V. M. Parakkat, G. M. Macauley, R. L. Stamps, and K. M. Krishnan, Configurable artificial spin ice with site-specific local magnetic fields, Phys. Rev. Lett. **126**, 017203 (2021).

[11] W. C. Yue, Z. Yuan, Y. Y. Lyu, S. Dong, J. Zhou, Z. L. Xiao, L. He, X. Tu, Y. Dong, H. Wang, W. Xu, L. Kang, P. Wu, C. Nisoli, W. K. Kwok, and Y. L. Wang, Crystallizing kagome artificial spin ice, Phys. Rev. Lett. **129**, 057202 (2022).

[12] D. Shi, H. Chen, J. Xu, H. Xia, Y. Chen, and Y. Wu, Kerr microscopy real-time imaging of the magnetization reversal process in kagome artificial spin ice, Phys. Rev. B. **101**, 134428 (2020).

[13] S. H. Skjærvø, C. H. Marrows, R. L. Stamps, and L. J. Heyderman, Advances in artificial spin ice, Nat. Rev. Phys. **2**, 13 (2020).

[14] L. J. Heyderman and R. L. Stamps, Artificial ferroic systems: Novel functionality from structure, interactions and dynamics, J. Phys. Condens. Matter **25**, 363201 (2013).

[15] Z. Budrikis, P. Politi, and R. L. Stamps, Vertex dynamics in finite two-dimensional square spin ices, Phys. Rev. Lett. **105**, 017201 (2010).

[16] N. Rougemaille, F. Montaigne, B. Canals, A. Duluard, D. Lacour, M. Hehn, R. Belkhou, O. Fruchart, S. El Moussaoui, A. Bendounan, and F. Maccherozzi, Artificial kagome arrays of nanomagnets: A frozen dipolar spin ice, Phys. Rev. Lett. **106**, 057209 (2011).

[17] S. Ladak, D. E. Read, G. K. Perkins, L. F. Cohen, and W. R. Branford, Direct observation of magnetic monopole defects in an artificial spin-ice system, Nat. Phys. **6**, 359 (2010).

[18] S. Zhang, I. Gilbert, C. Nisoli, G. W. Chern, M. J. Erickson, L. O'Brien, C. Leighton, P. E. Lammert, V. H. Crespi, and P. Schiffer, Crystallites of magnetic charges in artificial spin ice, Nature (London) **500**, 553 (2013).

[19] C. Nisoli, R. Wang, J. Li, W. F. McConville, P. E. Lammert, P. Schiffer, and V. H. Crespi, Ground state lost but degeneracy found: The effective thermodynamics of artificial spin ice, Phys. Rev. Lett. **98**, 217203 (2007).

[20] E. Mengotti, L. J. Heyderman, A. F. Rodríguez, F. Nolting, R. V. Hügli, and H. B. Braun, Real-space observation of emergent magnetic monopoles and associated Dirac strings in artificial kagome spin ice, Nat. Phys. **7**, 68 (2011).

[21] J. Colbois, K. Hofhuis, Z. Luo, X. Wang, A. Hrabec, L. J. Heyderman, and F. Mila, Artificial out-of-plane Ising antiferromagnet on the kagome lattice with very small farther-neighbor couplings, Phys. Rev. B. **104**, 024418 (2021).

[22] D. P. Landau and K. Binder, Phase diagrams and critical behavior of Ising square lattices with nearest-, next-nearest-, and third-nearest-neighbor couplings, Phys. Rev. B. **31**, 5946 (1985).

[23] D. Levis, L. F. Cugliandolo, L. Foini, and M. Tarzia, Thermal phase transitions in artificial spin ice, Phys. Rev. Lett. **110**, 207206 (2013).

[24] V.- D. Nguyen, Y. Perrin, S. Le Denmat, B. Canals, and N. Rougemaille, Competing interactions in artificial spin chains, Phys. Rev. B. **96**, 014402 (2017).

[25] S. Zhang, J. Li, J. Bartell, X. Ke, C. Nisoli, P. E. Lammert, V. H. Crespi, and P. Schiffer, Ignoring your neighbors: Moment correlations dominated by indirect or distant interactions in

an ordered nanomagnet array, Phys. Rev. Lett. **107**, 117204 (2011).

[26] O. Brunn, Y. Perrin, B. Canals, and N. Rougemaille, Signatures of farther neighbor couplings in artificial square ice, Phys. Rev. B. **103**, 094405 (2021).

[27] X. Ke, J. Li, S. Zhang, C. Nisoli, V. H. Crespi, and P. Schiffer, Tuning magnetic frustration of nanomagnets in triangular-lattice geometry, Appl. Phys. Lett. **93**, 252504 (2008).

[28] A. Smerald and F. Mila, Spin-liquid behaviour and the interplay between Pokrovsky-Talapov and Ising criticality in the distorted, triangular-lattice, dipolar Ising antiferromagnet, SciPost Phys. **5**, 030 (2018).

[29] Y. Shokef, A. Souslov, and T. C. Lubensky, Order by disorder in the antiferromagnetic Ising model on an elastic triangular lattice, PNAS **108**, 11804 (2011).

[30] V. Kapaklis, U. B. Arnalds, A. Farhan, R. Chopdekar, A. Balan, A. Scholl, L. J. Heyderman, and B. Hjörvarsson, Thermal fluctuations in artificial spin ice, Nat. Nanotechnol. **9**, 514 (2014).

[31] Y. Lao, F. Caravelli, M. Sheikh, J. Sklenar, D. Gardeazabal, J. D. Watts, A. M. Albrecht, A. Scholl, K. Dahmen, C. Nisoli, and P. Schiffer, Classical topological order in the kinetics of artificial spin ice, Nat. Phys. **14**, 723 (2018).

[32] L. Anghinolfi, H. Luetkens, J. Perron, M. G. Flokstra, O. Sendetskyi, A. Suter, T. Prokscha, P. M. Derlet, S. L. Lee, and L. J. Heyderman, Thermodynamic phase transitions in a frustrated magnetic metamaterial, Nat. Commun. **6**, 8278 (2015).

[33] A. Farhan, P. M. Derlet, A. Kleibert, A. Balan, R. V. Chopdekar, M. Wyss, J. Perron, A. Scholl, F. Nolting, and L. J. Heyderman, Direct observation of thermal relaxation in artificial spin ice, Phys. Rev. Lett. **111**, 057204 (2013).

[34] V. Schánilec, B. Canals, V. Uhlíř, L. Flajšman, J. Sadílek, T. Šikola, and N. Rougemaille, Bypassing dynamical freezing in artificial kagome ice, Phys. Rev. Lett. **125**, 057203 (2020).

[35] I. Gilbert, Y. Lao, I. Carrasquillo, L. O'Brien, J. D. Watts, M. Manno, C. Leighton, A. Scholl, C. Nisoli, and P. Schiffer, Emergent reduced dimensionality by vertex frustration in artificial spin ice, Nat. Phys. **12**, 162 (2016).

[36] Y. L. Wang, Z. L. Xiao, A. Snezhko, J. Xu, L. E. Ocola, R. Divan, J. E. Pearson, G. W. Crabtree, and W. K. Kwok, Rewritable artificial magnetic charge ice, Science **352**, 962 (2016).

[37] D. Shi, Z. Budrikis, A. Stein, S. A. Morley, P. D. Olmsted, G. Burnell, and C. H. Marrows, Frustration and thermalisation in an artificial magnetic quasicrystal, Nat. Phys. **14**, 309 (2018).

[38] E. Östman, H. Stopfel, I. A. Chioar, U. B. Arnalds, A. Stein, V. Kapaklis, and B. Hjörvarsson, Interaction modifiers in artificial spin ices, Nat. Phys. **14**, 375 (2018).

[39] Y. Perrin, B. Canals, and N. Rougemaille, Extensive degeneracy, Coulomb phase and magnetic monopoles in artificial square ice, Nature **540**, 410 (2016).

[40] G. Möller and R. Moessner, Artificial square ice and related dipolar nanoarrays, Phys. Rev. Lett. **96**, 237202 (2006).

[41] See Supplemental Material at http://link.aps.org/supplemental/10.1103/PhysRevB.108.184433 for detailed experiment and simulation methods description as well as the SEM and MFM images.

[42] M. J. Donahue and D. G. Porter, *OOMMF User's Guide, Version 1.0, Interagency Report NISTIR 6376* (National Institute of Standards and Technology, Gaithersburg, MD, 1999).